PNAS

Supporting Information for

Origami state machine with time-varying magnetic fields

Yifan Rao, Konstantinos Manos, Tuo Zhao, Minjie Chen, and Glaucio H. Paulino

Minjie Chen and Glaucio H. Paulino.
E-mail: minjie@princeton.edu, gpaulino@princeton.edu.

This PDF file includes:

Supporting text
Figs. S1 to S11
Tables S1 to S3
Legends for Movies S1 to S6
SI References

Other supporting materials for this manuscript include the following:

Movies S1 to S6

Supporting Information Text

1. Design, Fabrication, and Characterization of Origami State Machines

A. Unit Cell Design for Graded Energy Landscapes. The origami state machine is constructed from four types of Kresling origami unit cells (yellow, red, white, and black), each exhibiting distinct geometric (see Fig. S1) and material (Table S1) properties to achieve different energy barriers and bistable characteristics. All cells share identical hexagonal top and bottom surfaces with polygon edges of $N_p = 6$ and a circumscribed circle radius of $r = 9.8$ mm. To design these crease patterns shown in Fig. S1, the deployed heights $h_{\text{deploy}}^{\text{design}}$ and folded heights $h_{\text{fold}}^{\text{design}}$ are prescribed, as listed in Table S1. Given the two prescribed heights and the polygon geometry, all remaining geometric parameters labeled in Fig. S1, are uniquely determined through the kinematic constraints described by Eqs. 7-9. To achieve programmable energy landscapes, four paper materials with distinct properties are used to fabricate the unit cells (Table S1). The combination of geometric variation and material grading enables the design of unit cells with graded energy landscapes.

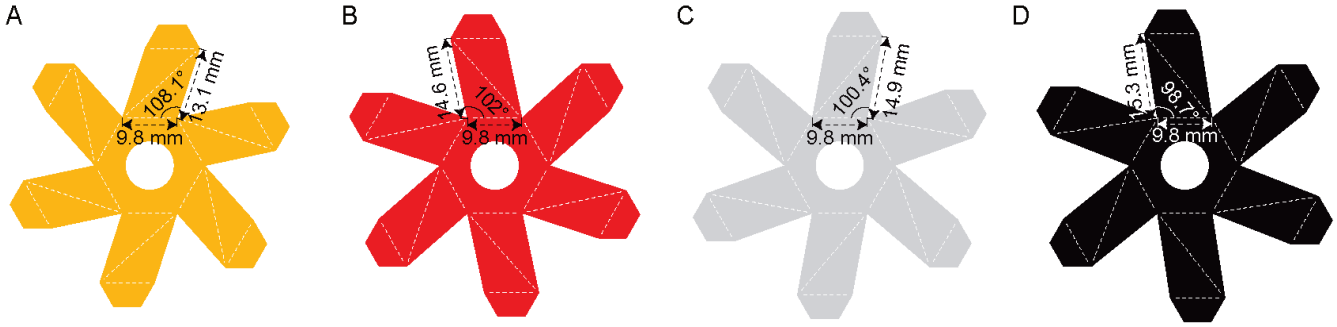


Fig. S1. Crease patterns and corresponding geometric parameters of the four Kresling origami unit cells used in this study: (A) yellow, (B) red, (C) white, and (D) black.

Table S1. Design, materials, and key parameters of the Kresling origami unit cells used in this study.

Parameter	Symbol	Unit	Red cell	Yellow cell	Black cell	White cell	Light blue cell (simulation-only)
Geometric Parameters							
Polygon edges	N_p	—	6	6	6	6	6
Circumscribed radius of hexagon	r	mm	9.8	9.8	9.8	9.8	9.8
Deployed height (design)	$h_{\text{deploy}}^{\text{design}}$	mm	14.0	11.6	15.0	14.5	N/A
Folded height (design)	$h_{\text{fold}}^{\text{design}}$	mm	0	0	0	0	N/A
Deployed height (calibrated)[a]	h_{deploy}	mm	13.8	11.1	14.0	13.86	13.8
Folded height (calibrated)[a]	h_{fold}	mm	4.9	3.05	6.5	6.2	4.9
Material Properties							
Paper type	—	—	Taro	Copy	Canson	Mixed Media	N/A
Thickness	t	mm	0.13	0.118	0.23	0.21	N/A
Unit cell mass[b]	m^{eff}	g	0.33151	0.28386	0.4059	0.22535	0.33151
Unit cell moment of inertia[b]	J^{eff}	N·mm^2	0.01327	0.01136	0.01624	0.009018	0.01327
Experimental Torsional Parameters							
Chirality	C	—	$LH(+1)$	$RH(-1)$	$LH(+1)$	$RH(-1)$	$LH(+1)$
Peak torque	T_{p}	N·mm	2.4741	1.2723	5.2228	4.6652	N/A
Minimum torque	T_{m}	N·mm	−1.2789	0.568	−1.3071	−1.3658	N/A
Snap-through twist angle	φ_{s}	deg	26.4857	18.7291[c]	30.4614	32.153	N/A
Twist angle at 2$^{\text{nd}}$ stable (folded) state	φ_{f}	deg	48.3343	40[c]	45.6141	44.6046	N/A
Calibrated Stiffness[d]							
Stretching stiffness of the mountain crease	$k_{s,b}$	N/mm	1.1026	1.2066	2.9119	2.6102	1.6539
Rotational stiffness along the mountain crease	$k_{r,b}$	N·mm/rad	0.0294	0.0195	0.1035	0.0849	0.0441

[a]Calibrated heights account for practical folding limitations and are used in dynamical simulations.
[b]The effective mass is calibrated using a lumped mass model, and the effective moment of inertia is derived from the resulting mass distribution (see more details in Section 5B).
[c]For the yellow cell, the twist angle at minimum torque is taken as the snap-through twist angle, and the twist angle in the folded state is obtained from manual measurement (see more details in Section 5A).
[d]Stiffnesses are calibrated by matching torsional test results with quasi-static model predictions (see more details in Section 5A).

B. Fabrication and Vertical Assembly. Unit cells are fabricated by laser cutting crease patterns into the respective paper materials, followed by manual folding along prescribed mountain and valley folds. Individual cells are assembled into vertical columns using custom-designed hexagonal connecting plates (thickness 0.5 mm), fabricated via a Stratasys J55 PolyJet 3D printer with VeroUltra™ White (RGD825). For the four-cell origami state machine shown in the Main Text, the cells are arranged from bottom to top in the order red, yellow, black, and white, with alternating chirality LH–RH–LH–RH. A cylindrical NdFeB permanent magnet (grade N45; diameter 9.525 mm; thickness 3.175 mm; mass 1.704 g), magnetized in-plane ($M_0 = 1.05 \times 10^6$ A/m), is mounted at the center of the top plate to enable magnetic actuation.

C. Quasi-Static Torsional Test. To characterize the energy barrier of each unit cell, quasi-static torsional tests are performed on individual cells using an Instron Model 68SC-5 Single Column Testing System equipped with a force/torque sensor (capacity: ±445 N axial, ±5.65 N · m torsional) (Fig. S2). The unit cell is mounted between two rigid plates with the bottom plate fixed and the top plate subjected to a controlled rotational displacement at 0.5 deg/s. During testing, the cell undergoes free axial translation to accommodate height changes during folding via a custom-designed free-translational fixture (1). The torque and axial force are simultaneously recorded to identify the energy barrier and stiffness (further analysis is provided in Section 5A).

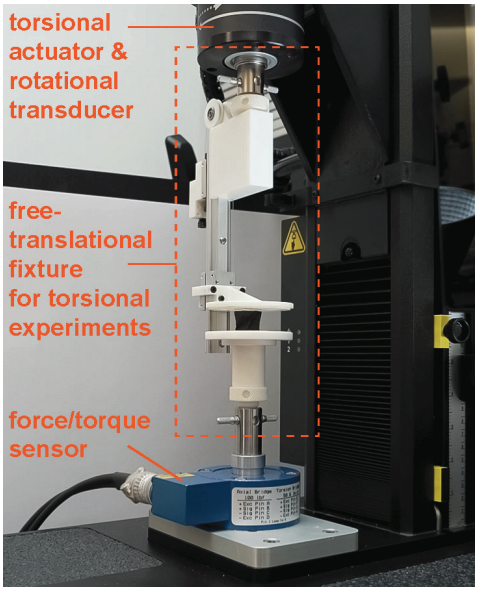


Fig. S2. Experimental setup for quasi-static torsional testing of an individual Kresling origami unit cell with free axial translation.

2. Deterministic State Transitions: Full-State Reachability, Graph Construction, and Shortest Paths

A. Full-State Reachability for Arbitrary n. Here we provide a constructive proof of the full-state reachability theorem stated in the Main Text. Specifically, we show that, for an arbitrary n-cell assembly with any chirality pattern $\mathbf{C} \in \{+1, -1\}^n$ and mutually distinct energy barriers, any target configuration $\mathbf{S}^{\text{target}}$ is reachable from any initial configuration through a finite sequence of binary actuation inputs. It is worth noting that *mutually distinct* is used in an operational sense, referring to distinguishable energy barriers during the state-transition process, such that only the compatible cell with the lowest energy barrier changes its state under a single actuation step.

For cell i, compatibility with an actuation step σ is given by Eq. 1 of the Main Text:

$$\chi_i(\sigma, S_i) = 1 \quad \Longleftrightarrow \quad \sigma = C_i(2S_i - 1). \tag{1}$$

Thus, for a given state S_i and chirality C_i, there exists a unique actuation direction under which cell i can change its state.

Starting from an arbitrary configuration $\mathbf{S}$, we compare it with the target configuration $\mathbf{S}^{\text{target}}$. Among all mismatched cells ($S_i \neq S_i^{\text{target}}$), we select the one with the largest energy barrier,

$$i_h = \underset{S_i \neq S_i^{\text{target}}}{\arg\max}\ \Delta U_i. \tag{2}$$

If $\mathbf{S} = \mathbf{S}^{\text{target}}$, then the target configuration has been reached. Otherwise, we apply the unique compatible actuation direction

$$\sigma_h = C_{i_h}(2S_{i_h} - 1), \tag{3}$$

under which cell i_h is compatible.

Under repeated application of σ_h, the deterministic transition rule (Eq. 2 of the Main Text) always selects the compatible cell with the lowest energy barrier. Therefore, before cell i_h changes state, only compatible cells with lower energy barriers may undergo state transitions. Once such a cell changes state, Eq. 1 immediately makes it incompatible with the same actuation direction, preventing it from being actuated again while σ_h is maintained. Since only finitely many compatible cells possess lower energy barriers than ΔU_{i_h}, they are exhausted after finitely many transition events. Cell i_h then becomes the compatible cell with the lowest energy barrier and therefore changes its state, reaching its target configuration.

The current configuration is then updated and compared again with the target configuration. If mismatched cells remain, the mismatched cell with the highest energy barrier is selected and the same procedure is repeated. Since every subsequent programming cycle considers only mismatched cells with lower energy barriers, any cell that has already reached its target state can never be actuated again. Thus, each programming cycle permanently removes exactly one mismatch. Because the number of cells is finite, the procedure terminates after finitely many cycles with $\mathbf{S} = \mathbf{S}^{\text{target}}$. Since both the initial and target configurations are arbitrary, every target configuration is reachable from every initial configuration.

B. Construction of the State-Transition Graph. The corresponding deterministic state-transition graph $\mathcal{G} = (\mathcal{V}, \mathcal{E})$ is obtained by enumerating the transition map $\mathcal{T}(\mathbf{S}, \sigma)$ over all 2^n configurations and both actuation directions:

$$\mathcal{V} = \{0,1\}^n, \qquad \mathcal{E} = \Big\{ \big(\mathbf{S},\, \mathcal{T}(\mathbf{S},\sigma)\big) : \mathbf{S} \in \mathcal{V},\ \sigma \in \{+1,-1\} \Big\}. \tag{4}$$

Each stable configuration corresponds to one node in the graph, giving $|\mathcal{V}| = 2^n$ nodes in total. For every node, $\mathcal{T}(\mathbf{S}, \sigma)$ is evaluated under both actuation directions ($\sigma = \pm 1$), producing two deterministic outgoing transitions when considering mutually distinct energy barriers. Consequently, the graph contains $|\mathcal{E}| = 2^{n+1}$ directed edges. Configurations satisfying $\mathcal{T}(\mathbf{S}, \sigma) = \mathbf{S}$ are represented by self-loops in the graph, corresponding to the equilibrium configurations derived in the Main Text. Figure S3 illustrates the complete deterministic state-transition graphs for origami state machines with n varying from 1 to 4 unit cells considering mutually distinct energy barriers (assumption). The resulting graph shows that every configuration is reachable from every other configuration via directed paths, consistent with the proof above.

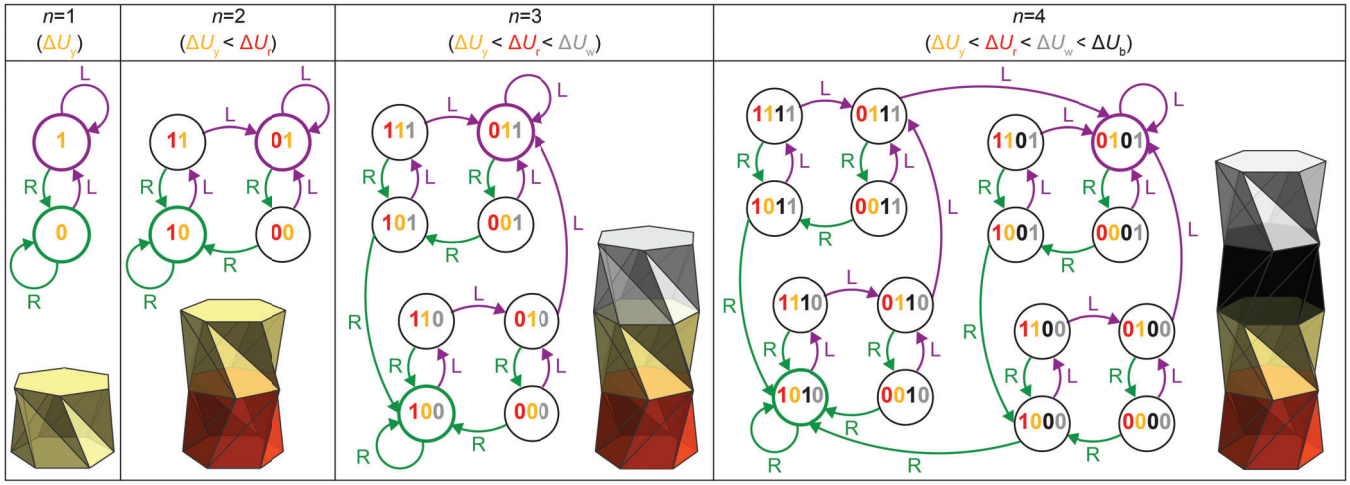


Fig. S3. Deterministic state-transition graphs for origami state machines with n varying from 1 to 4 unit cells considering mutually distinct energy barriers (assumption).

C. Shortest Paths via Breadth-First Search on $\mathcal{G}$. The minimum actuation sequence between any two configurations is obtained by breadth-first search (BFS) on $\mathcal{G}$. The algorithm is independent of the starting point: given a source configuration $\mathbf{S}^{\text{src}}$, BFS proceeds in rounds. Round 0 contains only $\mathbf{S}^{\text{src}}$. In each subsequent round k, both L and R actuations are applied to every configuration in round $k-1$, and any resulting configuration not encountered in earlier rounds is recorded at distance k and added to round k. Because each configuration is recorded at its earliest occurrence, the round in which $\mathbf{S}^{\text{target}}$ first appears equals the minimum number of actuation steps required to reach it; otherwise, a shorter path would have produced it in an earlier round, yielding a contradiction. This gives the shortest-path distance

$$d(\mathbf{S}^{\text{src}}, \mathbf{S}^{\text{target}}) = \min\big\{ k \geq 0 : \mathbf{S}^{\text{target}} \text{ first appears in round } k \big\}. \tag{5}$$

The minimum sequence $(\sigma_1, \ldots, \sigma_{k^*})$ is recovered by recording, for each newly reached configuration, its predecessor and the actuation (L or R) that produced it, and then back-tracing from $\mathbf{S}^{\text{target}}$ to $\mathbf{S}^{\text{src}}$. Self-loops at equilibrium nodes are automatically ignored, since an equilibrium is already recorded when first visited and thus never re-entered in subsequent rounds. This algorithm is applied in two ways. First, taking each equilibrium as $\mathbf{S}^{\text{src}}$ yields the shortest-path distances (k^*) and minimum sequences to all 16 target configurations, as tabulated in Table S2. Second, taking every configuration as $\mathbf{S}^{\text{src}}$ yields the complete 16×16 distance matrix D, tabulated in Table S3, from which $k^*_{\text{direct}} = d(\mathbf{S}^{\text{initial}}, \mathbf{S}^{\text{target}})$ is obtained directly for any given initial state.

Table S2. Shortest-path distances k^* and corresponding actuation sequences from each equilibrium to all 16 target configurations.

Target	From 0101 (L-equilibrium)		From 1010 (R-equilibrium)	
	k^*	Sequence	k^*	Sequence
0101	0	—	4	LLLL
0001	1	R	5	LLLLR
1001	2	RR	6	LLLLRR
1000	3	RRR	7	LLLLRRR
1101	3	RRL	7	LLLLRRL
1100	4	RRRL	8	LLLLRRRL
1010	4	RRRR	0	—
0100	5	RRRLL	9	LLLLRRRLL
1110	5	RRRRL	1	L
0000	6	RRRLLR	10	LLLLRRRLLR
0110	6	RRRRLL	2	LL
0010	7	RRRRLLR	3	LLR
0111	7	RRRRLLL	3	LLL
0011	8	RRRRLLLR	4	LLLR
1011	9	RRRRLLLRR	5	LLLRR
1111	10	RRRRLLLRRL	6	LLLRRL

Table S3. Full 16×16 shortest-path distance matrix D for the four-cell assembly. Entry D_{ij} gives the minimum number of L/R actuation steps (k^*_{direct}) from row state $\mathbf{S}^{\text{initial}}$ to column state $\mathbf{S}^{\text{target}}$.

$\mathbf{S}^{\text{initial}} \backslash \mathbf{S}^{\text{target}}$	0000	1000	0100	1100	0010	1010	0110	1110	0001	1001	0101	1101	0011	1011	0111	1111
0000	0	1	1	2	5	2	4	3	3	4	2	5	6	7	5	8
1000	3	0	2	1	4	1	3	2	4	5	3	6	5	6	4	7
0100	1	2	0	3	6	3	5	4	2	3	1	4	7	8	6	9
1100	2	1	1	0	5	2	4	3	3	4	2	5	6	7	5	8
0010	9	6	8	7	0	1	1	2	4	5	3	6	3	4	2	5
1010	10	7	9	8	3	0	2	1	5	6	4	7	4	5	3	6
0110	8	5	7	6	1	2	0	3	3	4	2	5	2	3	1	4
1110	9	6	8	7	2	1	1	0	4	5	3	6	3	4	2	5
0001	5	2	4	3	6	3	5	4	0	1	1	2	7	8	6	9
1001	4	1	3	2	5	2	4	3	3	0	2	1	6	7	5	8
0101	6	3	5	4	7	4	6	5	1	2	0	3	8	9	7	10
1101	5	2	4	3	6	3	5	4	2	1	1	0	7	8	6	9
0011	8	5	7	6	5	2	4	3	3	4	2	5	0	1	1	2
1011	9	6	8	7	4	1	3	2	4	5	3	6	3	0	2	1
0111	7	4	6	5	6	3	5	4	2	3	1	4	1	2	0	3
1111	8	5	7	6	5	2	4	3	3	4	2	5	2	1	1	0

3. Three-Dimensional Magnetic Actuation System and Field Control

A. 3D Helmholtz Coil System. Magnetic actuation is achieved using a custom-built three-dimensional (3D) Helmholtz coil system (2). As shown in Fig. S4A, the system consists of three orthogonal pairs of coils aligned with the x-, y-, and z-axes, enabling full control of the magnitude and orientation of time-varying magnetic fields via prescribed coil currents $(I_{XF},, I_{XB},, I_{YL},, I_{YR},, I_{ZT},, I_{ZB})$. A modular DC/AC power electronic converter drives the six coils independently. The required coil currents are computed on an NVIDIA Jetson AGX Orin computer and transmitted to the power electronics via a CAN bus interface. The system is powered by a 5-kW supply (BK Precision MR160120) providing a DC voltage of 55 V. Coil currents are measured using current probes (Tektronix A622) and recorded with a 6-channel oscilloscope (Tektronix MSO46B). Real-time system monitoring can be performed using mounted cameras, e-con Systems NileCAM25 (Fig. S4A).

B. Field–Current Mapping for Magnetic Actuation. To generate spatially uniform in-plane magnetic fields, each pair of coaxial coils is driven with equal currents in the same direction, i.e., $I_{XF} = I_{XB}$, $I_{YL} = I_{YR}$, and $I_{ZT} = I_{ZB}$ (2). The resulting magnetic field $\mathbf{B}(x, y, z, t) = [B_x, B_y, B_z]^{\mathrm{T}}$, where B_x, B_y, and B_z denote the field components along the x-, y-, and z-axes, is linearly related to the coil currents as,

$$\mathbf{B}(x, y, z, t) = \mathbf{A}(x, y, z)\, \mathbf{I}(t), \qquad [6]$$

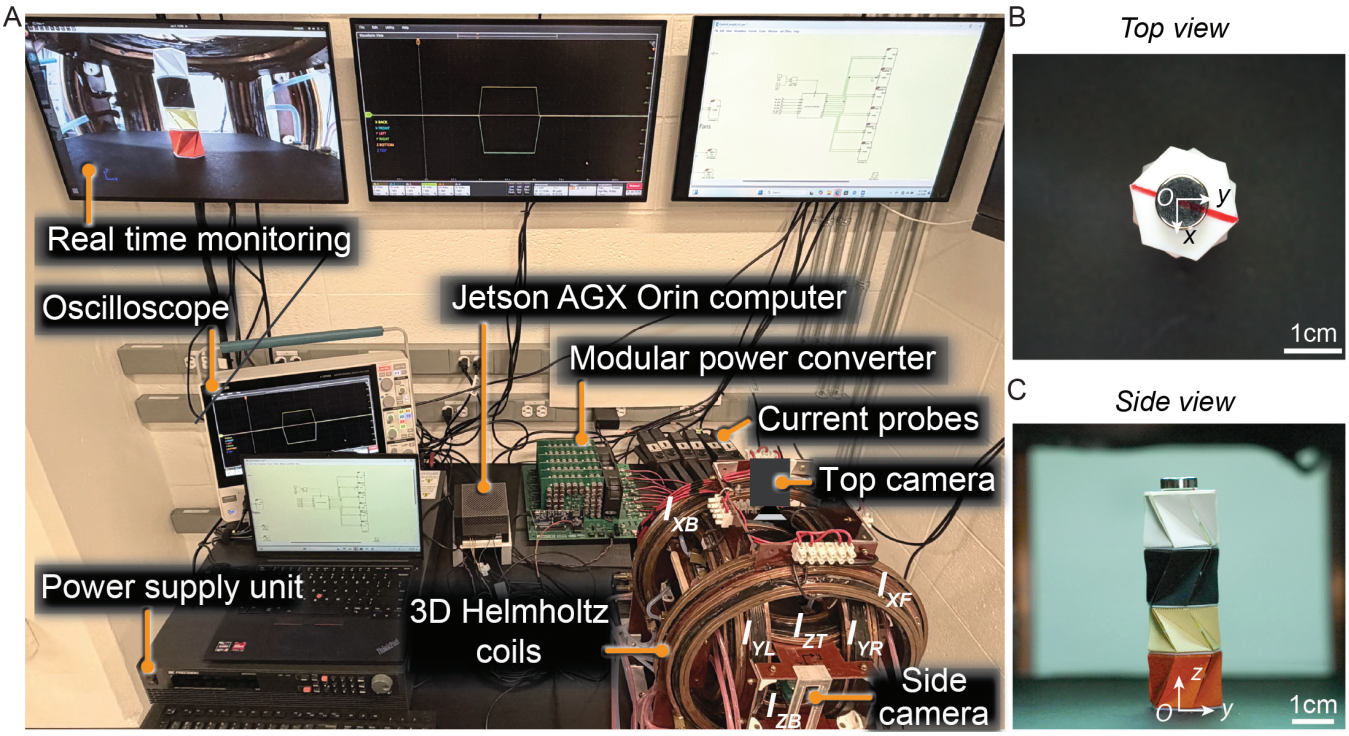


Fig. S4. Magnetic actuation system. (A) Custom-built 3D Helmholtz coil system. (B) Top view and (C) side view of the four-cell origami assembly positioned at coil system origin.

where $\mathbf{I} = [I_{XF}, I_{XB}, I_{YL}, I_{YR}, I_{ZT}, I_{ZB}]^{\mathrm{T}}$ is the current vector. At the origin of the coil system (Fig. S4B,C), the field–current mapping matrix is given by

$$\mathbf{A}(0,0,0) = \begin{bmatrix} 0.326 & 0.326 & 0 & 0 & 0 & 0 \\ 0 & 0 & 0.322 & 0.322 & 0 & 0 \\ 0 & 0 & 0 & 0 & 0.322 & 0.322 \end{bmatrix} \quad [\mathrm{mT/A}].$$

This matrix is determined from the coil geometry, electrical characteristics, and electromagnetic modeling, as detailed in (2).

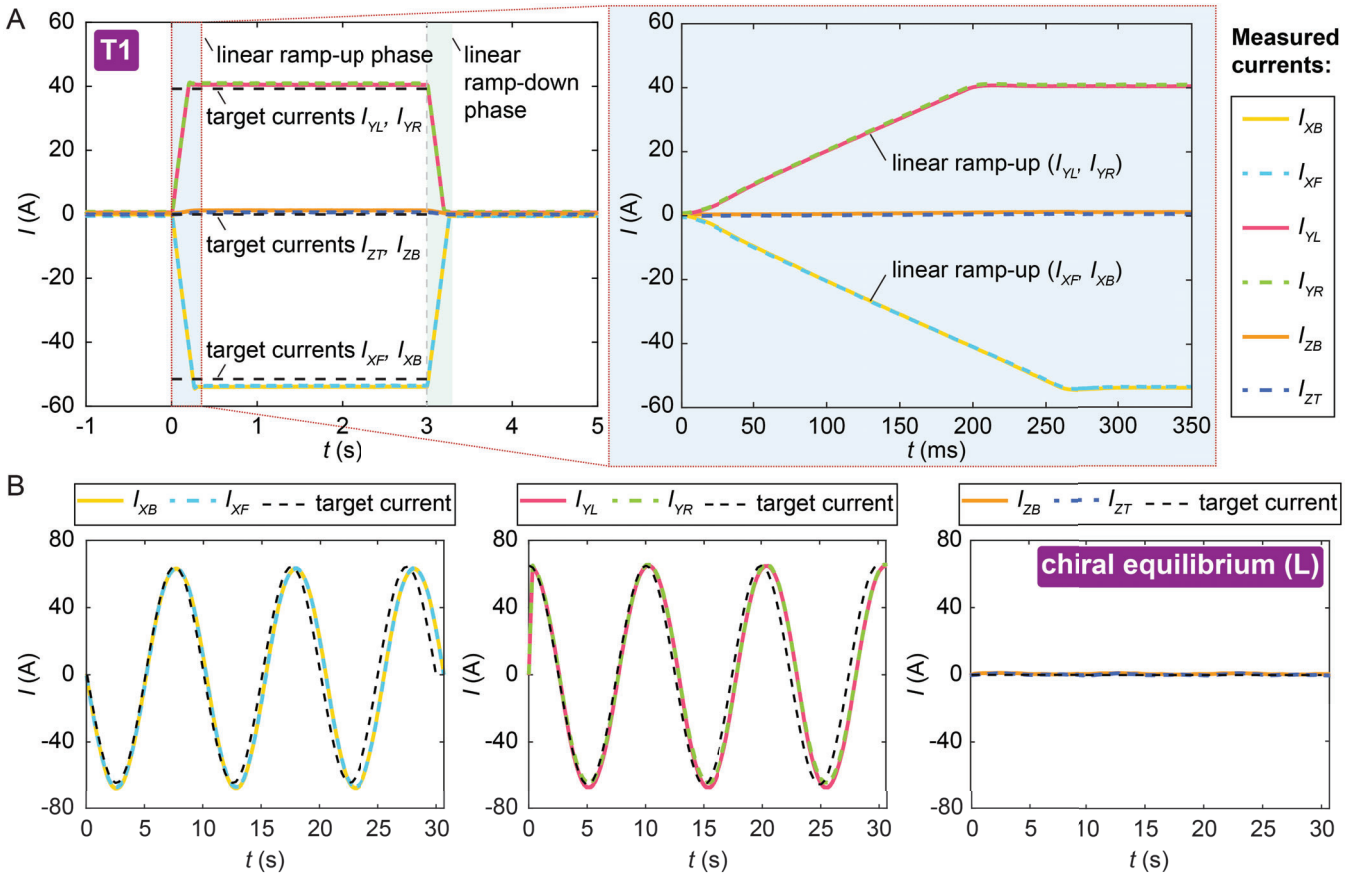


Fig. S5. Coil currents for pulsed and rotating magnetic actuation. (A) Measured and target currents for a pulsed magnetic field (T1) with $B_0 = 42$ mT and $\beta = 143°$, implemented using a linear ramping strategy. (B) Measured currents for ccw rotating magnetic fields with $B_0 = 42$ mT, $\beta_0 = 90°$, and $f = 0.1$ Hz generated using the same approach.

For in-plane actuation ($B_z = 0$), the pulsed magnetic field is parameterized by its magnitude $B_0 = \sqrt{B_x^2 + B_y^2}$ and orientation $\beta = \mathrm{atan2}(B_y, B_x)$. Given (B_0, β), the corresponding coil currents are obtained from Eq. 6. For rotating fields, the orientation evolves as $\beta(t) = \beta_0 + 2\pi f t$, where β_0 is the initial field orientation and f is the rotation frequency, while maintaining a constant magnitude B_0. The corresponding time-varying input currents are then computed using the same linear mapping in Eq. 6. As an example, Fig. S5A shows the six coil currents used to generate a pulsed magnetic field (transition T1) with $B_0 = 42$ mT and $\beta = 143°$ applied over a duration of $t_{\mathrm{duration}} = 3$ s. The target currents are computed from Eq. 6 and implemented using a linear ramping strategy, consisting of a ramp-up phase, a constant plateau, and a ramp-down phase. The measured currents closely follow the prescribed profiles, demonstrating accurate realization of the desired pulsed magnetic field. The finite ramp rate of the system results in a ramp time of approximately 300 ms, which is incorporated in the simulations (Fig. S5A). The same approach is used to generate rotating magnetic fields. As shown in Fig. S5B, the measured currents closely follow the prescribed sinusoidal profiles after an initial ramping transient, enabling continuous ccw rotation of an in-plane magnetic field with $B_0 = 42$ mT, $\beta_0 = 90°$, and $f = 0.1$ Hz.

C. State Identification via Imaging. State transitions are identified from imaging by tracking the orientation and vertical position of the top plate. The top view (Sony ILCE-9M2, 120 fps) is used to measure in-plane rotation (Fig. S4B), while the side view (Sony ILME-FX6V, 240 fps) captures height variations (Fig. S4C). As shown in Fig. S6, side-view image dimensions are calibrated using a 145 mm reference width. The vertical positions of the top and bottom plates are automatically detected using a custom Python script, and their difference defines the instantaneous system height. A similar procedure is used to extract the twist angle from the top-view recordings. These signals are used to identify discrete states and transition trajectories.

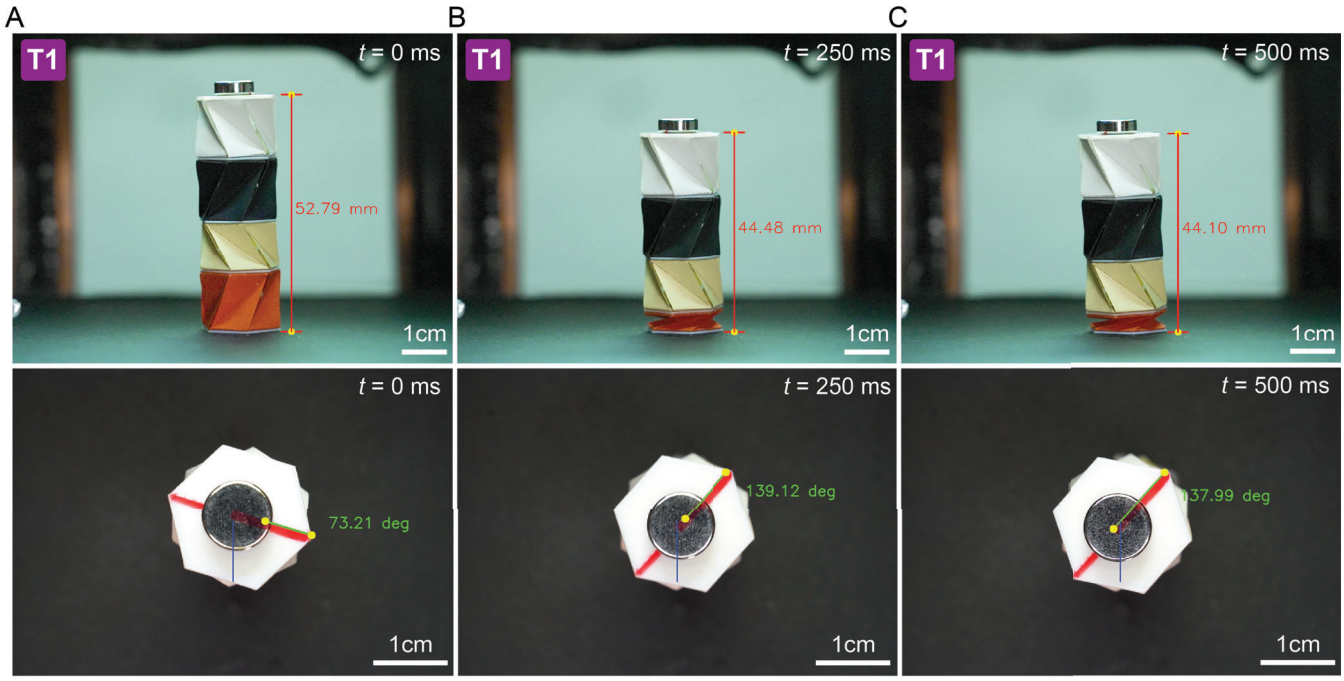


Fig. S6. Image-based height and twist-angle extraction from synchronized side-view and top-view recordings. Representative frames at $t = 0$, 250 ms, and 500 ms during transition T1 illustrate the detection of the top and bottom plates for height measurement and extraction of the twist angle from the orientation of the red magnetization marker.

D. Practical Considerations for Magnetic Actuation. The present experiments employ a calibrated Helmholtz-coil system to generate spatially uniform magnetic fields for reproducible characterization of the proposed actuation strategy. Practical deployment, however, introduces several additional considerations.

First, the present framework achieves deterministic state selection within an individual origami state machine. Identical origami state machines located within the same uniform magnetic field experience identical magnetic inputs and therefore respond identically. Independent control over multiple assemblies would require an additional selection mechanism, such as distinct actuation criteria or spatially selective magnetic fields.

Second, each embedded permanent magnet generates a magnetic dipole field that may couple neighboring origami state machines. For the permanent magnet used in this work ($VM_0 \approx 0.24\ \mathrm{A\,m^2}$), the maximum on-axis dipole field falls below 1 mT at center-to-center separations greater than approximately 3.6 cm (3), which is small relative to the 42 mT actuation field used here. At closer spacing, the associated field gradients may additionally induce translational forces or bending of the compliant origami assembly.

Third, nearby ferromagnetic objects can distort the magnitude and orientation of the applied magnetic field and introduce spatial field gradients, thereby shifting the effective operating point in the (B_0, δ) actuation space and reducing the reliability of deterministic state transitions.

Fourth, the present Helmholtz-coil system provides an approximately 15 cm-scale uniform-field region, substantially larger than the ~ 2 cm four-cell assembly used in this work (2). Larger origami state machines or simultaneous operation of multiple origami state machines would generally require larger or distributed magnetic-field generators.

Finally, the proposed state-transition framework is not intrinsically tied to the present Helmholtz-coil architecture. Alternative magnetic field sources, such as electromagnetic coil arrays or movable permanent magnets, could implement equivalent actuation protocols, provided that the local magnetic field satisfies the required actuation conditions (3).

4. Reduced-Order Dynamic Modeling of Magnetic Origami State Machines

We consider a n-unit Kresling origami assembly aligned along the positive z-axis, with one end ($i = 1$) rigidly fixed to the ground and the other end ($i = n$) remaining free. Here, i denotes the index of each unit cell. The Kresling structure of each unit cell consists of two identical, parallel, equilateral polygons with $N_p^{(i)}$ sides, connected by $2N_p^{(i)}$ repeating triangular panels. The deployment state of the i-th unit is denoted by S_i, where $S_i = 1$ indicates the deployed state and $S_i = 0$ the folded state. Chirality is defined as $C_i = 1$ for LH chiral cells, which fold under ccw torques, and $C_i = -1$ for RH chiral cells, which fold under cw torques.

A. Geometry. The geometry of the i-th unit cell ($i = 1, \ldots, n$) is defined by three geometric parameters: the folded state height $h_{\mathrm{fold}}^{(i)}$, the deployed state height $h_{\mathrm{deploy}}^{(i)}$, and the circumscribed circle radius of the polygon $r^{(i)}$. Therefore, the relative angles between the top and bottom polygons in the deployed and folded states are given by (1)

$$\begin{cases} \theta_{\mathrm{deploy}}^{(i)} = C_i \cdot 2\arctan\left[2\sin\phi^{(i)} \dfrac{\sin\phi^{(i)}\sqrt{\cot^2\phi^{(i)}\csc^2\phi^{(i)} - [(h_{\mathrm{deploy}}^{(i)}/a^{(i)})^2 - (h_{\mathrm{fold}}^{(i)}/a^{(i)})^2]^2} - \cos\phi^{(i)}}{1+(h_{\mathrm{deploy}}^{(i)}/a^{(i)})^2-(h_{\mathrm{fold}}^{(i)}/a^{(i)})^2+[1-(h_{\mathrm{deploy}}^{(i)}/a^{(i)})^2+(h_{\mathrm{fold}}^{(i)}/a^{(i)})^2]\cos 2\phi^{(i)}}\right], \\ \theta_{\mathrm{fold}}^{(i)} = C_i \cdot 2\arctan\left[2\sin\phi^{(i)} \dfrac{\sin\phi^{(i)}\sqrt{\cot^2\phi^{(i)}\csc^2\phi^{(i)} - [(h_{\mathrm{deploy}}^{(i)}/a^{(i)})^2 - (h_{\mathrm{fold}}^{(i)}/a^{(i)})^2]^2} - \cos\phi^{(i)}}{1-(h_{\mathrm{deploy}}^{(i)}/a^{(i)})^2+(h_{\mathrm{fold}}^{(i)}/a^{(i)})^2+[1+(h_{\mathrm{deploy}}^{(i)}/a^{(i)})^2-(h_{\mathrm{fold}}^{(i)}/a^{(i)})^2]\cos 2\phi^{(i)}}\right], \end{cases} \quad [7]$$

respectively. Here, $\phi^{(i)} = \pi/N_p^{(i)}$, and $a^{(i)} = 2r^{(i)}\sin\phi^{(i)}$ that represents the side length of the polygon in the i-th unit. It should be noted that, in this analysis, we assume the polygons do not deform during reconfiguration, i.e., $a_{\mathrm{deploy}}^{(i)} = a_{\mathrm{fold}}^{(i)} = a^{(i)}$, due to the rigid connecting plates.

The geometry of a single unit cell are defined by three lengths and three dihedral angles: the polygon side length $a^{(i)}$, the mountain crease length $b^{(i)}$, the valley crease length $c^{(i)}$, the dihedral angle between triangular panels and polygons $\delta_a^{(i)}$, the dihedral angle between triangular panels intersecting at mountain creases $\delta_b^{(i)}$, and the dihedral angle between triangular panels intersecting at valley creases $\delta_c^{(i)}$. In the deployed state, there are (1)

$$\begin{cases} b_{\mathrm{deploy}}^{(i)} = \sqrt{{h_{\mathrm{deploy}}^{(i)}}^2 + 4{r^{(i)}}^2\sin^2(\theta_{\mathrm{deploy}}^{(i)}/2)}, \\ c_{\mathrm{deploy}}^{(i)} = \sqrt{{h_{\mathrm{deploy}}^{(i)}}^2 + 4{r^{(i)}}^2\sin^2(\theta_{\mathrm{deploy}}^{(i)}/2 + C_i\cdot\phi^{(i)})}, \\ \delta_{a-\mathrm{deploy}}^{(i)} = \arctan\dfrac{h_{\mathrm{deploy}}^{(i)}}{2r^{(i)}\sin(\theta_{\mathrm{deploy}}^{(i)}/2+C_i\cdot\phi^{(i)})\sin(\theta_{\mathrm{deploy}}^{(i)}/2)}, \\ \delta_{b-\mathrm{deploy}}^{(i)} = \pi - \arccos\dfrac{{h_{\mathrm{deploy}}^{(i)}}^2\cos(\theta_{\mathrm{deploy}}^{(i)}+2C_i\cdot\phi^{(i)}) - {r^{(i)}}^2[\cos(\theta_{\mathrm{deploy}}^{(i)}+C_i\cdot\phi^{(i)})-\cos(\phi^{(i)})]^2}{{h_{\mathrm{deploy}}^{(i)}}^2+{r^{(i)}}^2[\cos(\theta_{\mathrm{deploy}}^{(i)}+C_i\cdot\phi^{(i)})-\cos(\phi^{(i)})]^2}, \\ \delta_{c-\mathrm{deploy}}^{(i)} = \pi - \arccos\dfrac{{h_{\mathrm{deploy}}^{(i)}}^2\cos(\theta_{\mathrm{deploy}}^{(i)}) - {r^{(i)}}^2[\cos(\theta_{\mathrm{deploy}}^{(i)}+C_i\cdot\phi^{(i)})-\cos(\phi^{(i)})]^2}{{h_{\mathrm{deploy}}^{(i)}}^2+{r^{(i)}}^2[\cos(\theta_{\mathrm{deploy}}^{(i)}+C_i\cdot\phi^{(i)})-\cos(\phi^{(i)})]^2}; \end{cases} \quad [8]$$

while in the folded state, there are

$$\begin{cases} b_{\text{fold}}^{(i)} = \sqrt{{h_{\text{fold}}^{(i)}}^2 + 4{r^{(i)}}^2 \sin^2(\theta_{\text{fold}}^{(i)}/2)}, \\ c_{\text{fold}}^{(i)} = \sqrt{{h_{\text{fold}}^{(i)}}^2 + 4{r^{(i)}}^2 \sin^2(\theta_{\text{fold}}^{(i)}/2 + C_i \cdot \phi^{(i)})}, \\ \delta_{a-\text{fold}}^{(i)} = \arctan \frac{h_{\text{fold}}^{(i)}}{2r^{(i)} \sin(\theta_{\text{fold}}^{(i)}/2 + C_i \cdot \phi^{(i)}) \sin(\theta_{\text{fold}}^{(i)}/2)}, \\ \delta_{b-\text{fold}}^{(i)} = \pi - \arccos \frac{{h_{\text{fold}}^{(i)}}^2 \cos(\theta_{\text{fold}}^{(i)} + 2C_i \cdot \phi^{(i)}) - {r^{(i)}}^2 [\cos(\theta_{\text{fold}}^{(i)} + C_i \cdot \phi^{(i)}) - \cos(\phi^{(i)})]^2}{{h_{\text{fold}}^{(i)}}^2 + {r^{(i)}}^2 [\cos(\theta_{\text{fold}}^{(i)} + C_i \cdot \phi^{(i)}) - \cos(\phi^{(i)})]^2}, \\ \delta_{c-\text{fold}}^{(i)} = \pi - \arccos \frac{{h_{\text{fold}}^{(i)}}^2 \cos(\theta_{\text{fold}}^{(i)}) - {r^{(i)}}^2 [\cos(\theta_{\text{fold}}^{(i)} + C_i \cdot \phi^{(i)}) - \cos(\phi^{(i)})]^2}{{h_{\text{fold}}^{(i)}}^2 + {r^{(i)}}^2 [\cos(\theta_{\text{fold}}^{(i)} + C_i \cdot \phi^{(i)}) - \cos(\phi^{(i)})]^2}. \end{cases} \quad [9]$$

For simplicity, we assume identical geometry across all units, i.e., $r^{(i)} = r$, $N_p^{(i)} = N_p$, $h_{\text{fold}}^{(i)} = h_{\text{fold}}$, $h_{\text{deploy}}^{(i)} = h_{\text{deploy}}$. Therefore, with the aid of Eqs. 7-9, the initial configuration of the i-th unit cell ($i = 1, \ldots, n$) is determined as

$$\begin{cases} a_0^{(i)} = a, \\ b_0^{(i)} = S_i \cdot b_{\text{deploy}} + (1 - S_i) \cdot b_{\text{fold}}, \\ c_0^{(i)} = S_i \cdot c_{\text{deploy}} + (1 - S_i) \cdot c_{\text{fold}}, \\ h_0^{(i)} = S_i \cdot h_{\text{deploy}} + (1 - S_i) \cdot h_{\text{fold}}, \\ \theta_0^{(i)} = S_i \cdot \theta_{\text{deploy}} + (1 - S_i) \cdot \theta_{\text{fold}}, \\ \delta_{a0}^{(i)} = S_i \cdot \delta_{a-\text{deploy}} + (1 - S_i) \cdot \delta_{a-\text{fold}}, \\ \delta_{b0}^{(i)} = S_i \cdot \delta_{b-\text{deploy}} + (1 - S_i) \cdot \delta_{b-\text{fold}}, \\ \delta_{c0}^{(i)} = S_i \cdot \delta_{c-\text{deploy}} + (1 - S_i) \cdot \delta_{c-\text{fold}}. \end{cases} \quad [10]$$

B. Kinematics. The folding and deployment behavior of the i-th unit cell is governed by two independent variables: the axial displacement u_i and the twisting angle φ_i of the top polygon. To analyze the kinematics of the origami assembly, we derive the following relationships (1):

$$\begin{cases} b_i(\Delta u_i, \Delta\varphi_i) = \sqrt{h_i^2 + 4r^2 \sin^2(\theta_i/2)}, \\ c_i(\Delta u_i, \Delta\varphi_i) = \sqrt{h_i^2 + 4r^2 \sin^2(\theta_i/2 + C_i \cdot \phi)}, \\ \delta_a^i(\Delta u_i, \Delta\varphi_i) = \arctan \frac{h_i}{2r \sin(\theta_i/2 + C_i \cdot \phi) \sin(\theta_i/2)}, \\ \delta_b^i(\Delta u_i, \Delta\varphi_i) = \pi - \arccos \frac{h_i^2 \cos(\theta_i + 2C_i \cdot \phi) - r^2 [\cos(\theta_i + C_i \cdot \phi) - \cos(\phi)]^2}{h_i^2 + r^2 [\cos(\theta_i + C_i \cdot \phi) - \cos(\phi)]^2}, \\ \delta_c^i(\Delta u_i, \Delta\varphi_i) = \pi - \arccos \frac{h_i^2 \cos(\theta_i) - r^2 [\cos(\theta_i + C_i \cdot \phi) - \cos(\phi)]^2}{h_i^2 + r^2 [\cos(\theta_i + C_i \cdot \phi) - \cos(\phi)]^2}, \end{cases} \quad [11]$$

where $h_i = h_0^{(i)} + \Delta u_i$ and $\theta_i = \theta_0^{(i)} + \Delta\varphi_i$ represent the height and relative angle between the top and bottom polygons of the i-th unit in the deformed configuration. The relative axial displacement and rotation between adjacent units are defined as $\Delta u_i = u_i - u_{i-1}$ and $\Delta\varphi_i = \varphi_i - \varphi_{i-1}$, respectively. For reference, the displacement and rotation of the virtual 0-th unit are set to zero, that is, $u_0 = 0$ and $\varphi_0 = 0$, which represents the bottom unit ($n = 1$) being fixed.

C. Elastic Potential Energy. Inspired by the bar-and-hinge model for Kresling origami cells (4), we model each unit cell as a combination of bar elements and rotational springs. The total elastic energy of each unit consists of contributions from the axial deformation of the bar elements and the rotational deformation at the hinges. With the aid of Eqs. 10–11, the total elastic potential energy stored in the i-th unit is given by (1)

$$U_{\text{e}}^{(i)} = \frac{1}{2} N_p k_{s,b}^{(i)} (b_i - b_0^{(i)})^2 + \frac{1}{2} N_p k_{s,c}^{(i)} (c_i - c_0^{(i)})^2 + \frac{1}{2} (2N_p) k_{r,a}^{(i)} (\delta_a^i - \delta_{a0}^{(i)})^2 + \frac{1}{2} N_p k_{r,b}^{(i)} (\delta_b^i - \delta_{b0}^{(i)})^2 + \frac{1}{2} N_p k_{r,c}^{(i)} (\delta_c^i - \delta_{c0}^{(i)})^2, \quad [12]$$

where $k_{s,b}^{(i)} = k_s^{(i)}/b_0^{(i)}$, $k_{s,c}^{(i)} = k_s^{(i)}/c_0^{(i)}$, $k_{r,a}^{(i)} = k_r^{(i)} a_0^{(i)}$, $k_{r,b}^{(i)} = k_r^{(i)} b_0^{(i)}$, and $k_{r,c}^{(i)} = k_r^{(i)} c_0^{(i)}$. To avoid the intersection of adjacent panels near extreme folding or deployment states, we refine the definition of the rotational stiffness $k_r^{(i)}$ by introducing a piecewise continuous function of the dihedral angle $\delta_m^{(i)}$. Specifically, for each hinge type $m \in a, b, c$, the tangent rotational stiffness is designed to remain constant within a compliant range $[\delta_{m-\text{fold}}^{(i)}, \delta_{m-\text{deploy}}^{(i)}]$, and to diverge rapidly outside this range to reflect geometric and material constraints. The constitutive law is given by (4)

$$k_{r,\text{eff}}^{(i)}(\delta_m^{(i)}) = \begin{cases} k_r^{(i)} \sec^2\left(\dfrac{\pi(\delta_m^{(i)} - \delta_{m-\text{fold}}^{(i)})}{2\delta_{m-\text{fold}}^{(i)}}\right), & 0 < \delta_m^{(i)} < \delta_{m-\text{fold}}^{(i)}, \\ k_r^{(i)}, & \delta_{m-\text{fold}}^{(i)} \le \delta_m^{(i)} \le \delta_{m-\text{deploy}}^{(i)}, \\ k_r^{(i)} \sec^2\left(\dfrac{\pi(\delta_m^{(i)} - \delta_{m-\text{deploy}}^{(i)})}{2\pi - 2\delta_{m-\text{deploy}}^{(i)}}\right), & \delta_{m-\text{deploy}}^{(i)} < \delta_m^{(i)} \le \pi, \end{cases} \quad [13]$$

where the hinge-specific angular limits $\delta_{m-\text{fold}}^{(i)}$ and $\delta_{m-\text{deploy}}^{(i)}$ where $m \in a, b, c$ correspond to the fold and deploy thresholds, respectively. The parameters $k_s^{(i)}$ and $k_r^{(i)}$ are identified using the procedure described in Section 5A and reported in Table S1.

D. Magnetic Torque. The magnetization of the embedded permanent magnet in the initial configuration is described as

$$\mathbf{M} = M_0 \left[\cos\alpha,\, \sin\alpha,\, 0\right]^{\mathrm{T}}, \tag{14}$$

where M_0 is the magnetization magnitude and α denotes its initial orientation.

The applied in-plane magnetic field is parameterized by its magnitude B_0 and time-dependent orientation $\beta(t)$ as

$$\mathbf{B}(t) = B_0 \left[\cos\beta(t),\, \sin\beta(t),\, 0\right]^{\mathrm{T}}. \tag{15}$$

For pulsed magnetic fields, $\beta(t)$ is piecewise constant, while for rotating fields, $\beta(t) = \beta_0 + 2\pi f t$, where β_0 is the initial orientation and f is the rotation frequency.

As the permanent magnet rotates rigidly with the unit cell, the magnetization in the current configuration becomes (5)

$$\mathbf{m}(\varphi_n) = \mathbf{R}(\varphi_n)\mathbf{M} = M_0 \begin{bmatrix} \cos\varphi_n & -\sin\varphi_n & 0 \\ \sin\varphi_n & \cos\varphi_n & 0 \\ 0 & 0 & 1 \end{bmatrix} \begin{bmatrix} \cos\alpha \\ \sin\alpha \\ 0 \end{bmatrix} = M_0 \begin{bmatrix} \cos(\alpha+\varphi_n) \\ \sin(\alpha+\varphi_n) \\ 0 \end{bmatrix}, \tag{16}$$

where φ_n is the rotational angle of the top (n-th) cell, and $\mathbf{R}(\varphi_n)$ denotes the in-plane rotation matrix.

Assuming a magnet volume V, the magnetic potential energy is

$$U_{\mathrm{mag}}(\varphi_n) = -V\,\mathbf{m}(\varphi_n)\cdot\mathbf{B} = -V\,M_0\,B_0\,\cos(\beta_0 + 2\pi f t - \alpha - \varphi_n). \tag{17}$$

The resulting magnetic torque acting on φ_n is

$$\tau_{\mathrm{mag}}^{(n)} = -\frac{\partial U_{\mathrm{mag}}}{\partial \varphi_n} = V\,M_0\,B\,\sin(\beta_0 + 2\pi f t - \alpha - \varphi_n). \tag{18}$$

E. Equations of Motion. We develop the equations of motion for the magnetic origami state machine using Lagrangian mechanics (6). The total kinetic energy is

$$T = \tfrac{1}{2}\sum_{i=1}^{n} m_i^{\mathrm{eff}}\dot{u}_i^2 + \tfrac{1}{2}\sum_{i=1}^{n} J_i^{\mathrm{eff}}\dot{\varphi}_i^2, \tag{19}$$

where m_i^{eff} and J_i^{eff} denote the effective mass and moment of inertia of the i-th unit cell, as determined using the method described in Section 5B and reported in Table S1.

The total potential energy is

$$V = \sum_{i=1}^{n} U_{\mathrm{e}}^{(i)}, \tag{20}$$

where $U_{\mathrm{e}}^{(i)}$ is the elastic energy of the i-th unit (Eq. 12). The calibrated rest heights correspond to gravitational equilibrium configurations; thus, gravity is implicitly accounted for and omitted from the equations of motion.

Dissipation is modeled using a Rayleigh dissipation function,

$$D = \frac{1}{2}\sum_{i=1}^{n} \nu m_i^{\mathrm{eff}}\dot{u}_i^2 + \frac{1}{2}\sum_{i=1}^{n} \nu J_i^{\mathrm{eff}}\dot{\varphi}_i^2, \tag{21}$$

where ν is the damping factor, as calibrated using the method described in Section 5C. Energy dissipation in paper-folded Kresling cells arises from multiple mechanisms, including friction, hysteresis, crease plasticity, and rate-dependent effects. To efficiently predict the state-transition behavior of the origami state machine, we adopt the phenomenological linear viscous damping term to represent the combined influence of multiple dissipation mechanisms, consistent with previous studies on paper-based Kresling origami structures (7).

The Lagrangian is defined as

$$L = T - V. \tag{22}$$

The equations of motion for the i-th unit cell are obtained from Lagrange's equations as

$$\begin{cases} \frac{d}{dt}\left(\frac{\partial L}{\partial \dot{u}_i}\right) - \frac{\partial L}{\partial u_i} + \frac{\partial D}{\partial \dot{u}_i} = F_{\mathrm{ext}}^{(i)}, \\ \frac{d}{dt}\left(\frac{\partial L}{\partial \dot{\varphi}_i}\right) - \frac{\partial L}{\partial \varphi_i} + \frac{\partial D}{\partial \dot{\varphi}_i} = T_{\mathrm{ext}}^{(i)}, \end{cases} \tag{23}$$

where $F_{\mathrm{ext}}^{(i)}$ and $T_{\mathrm{ext}}^{(i)}$ are generalized external force and torque (1). In particular, the magnetic actuation enters as $T_{\mathrm{ext}}^{(n)} = \tau_{\mathrm{mag}}^{(n)}$ (Eq. 18), while $T_{\mathrm{ext}}^{(i)} = 0$ for $i < n$. Substituting Eqs. 18–22 into Eq. 23 yields the governing equations of motion

$$\begin{cases} m_i^{\mathrm{eff}}(\ddot{u}_i + \nu\dot{u}_i) = F_{\mathrm{mech}}^{(i+1)} - F_{\mathrm{mech}}^{(i)}, \\ J_i^{\mathrm{eff}}(\ddot{\varphi}_i + \nu\dot{\varphi}_i) = T_{\mathrm{mech}}^{(i+1)} - T_{\mathrm{mech}}^{(i)} + \tau_{\mathrm{mag}}^{(i)}, \end{cases} \tag{24}$$

where

$$\begin{cases} F_{\text{mech}}^{(i)} = \frac{\partial U_{\text{e}}^{(i)}}{\partial \Delta u_i} = N_p k_s \left(\frac{b_i}{b_0^{(i)}} - 1\right) \frac{h_i}{b_i} + N_p k_s \left(\frac{c_i}{c_0^{(i)}} - 1\right) \frac{h_i}{c_i} + \frac{2 N_p k_{r,\text{eff}}^{(i)} a_0^{(i)} (\delta_a^i - \delta_{a0}^{(i)})}{(1+\tan^2 \delta_a^i) 2r \sin(\theta_i/2 + C_i \cdot \phi) \sin(\theta_i/2)} \\ \qquad + \frac{N_p k_{r,\text{eff}}^{(i)} b_0^{(i)} (\delta_b^i - \delta_{b0}^{(i)})}{\sqrt{1-\cos^2 \delta_b^i}} \frac{\partial \cos(\pi - \delta_b^i)}{\partial \Delta u_i} + \frac{N_p k_{r,\text{eff}}^{(i)} c_0^{(i)} (\delta_c^i - \delta_{c0}^{(i)})}{\sqrt{1-\cos^2 \delta_c^i}} \frac{\partial \cos(\pi - \delta_c^i)}{\partial \Delta u_i}, \\ T_{\text{mech}}^{(i)} = \frac{\partial U_{\text{e}}^{(i)}}{\partial \Delta \varphi_i} = N_p k_s \left(\frac{b_i}{b_0^{(i)}} - 1\right) \frac{r^2 \sin \theta_i}{b_i} + N_p k_s \left(\frac{c_i}{c_0^{(i)}} - 1\right) \frac{r^2 \sin(\theta_i + 2C_i \cdot \phi)}{c_i} + \frac{2 N_p k_{r,\text{eff}}^{(i)} a_0^{(i)} (\delta_a^i - \delta_{a0}^{(i)})}{1+\tan^2 \delta_a^i} \frac{\partial \tan \delta_a^i}{\partial \Delta \varphi_i} \\ \qquad + \frac{N_p k_{r,\text{eff}}^{(i)} b_0^{(i)} (\delta_b^i - \delta_{b0}^{(i)})}{\sqrt{1-\cos^2 \delta_b^i}} \frac{\partial \cos(\pi - \delta_b^i)}{\partial \Delta \varphi_i} + \frac{N_p k_{r,\text{eff}}^{(i)} c_0^{(i)} (\delta_c^i - \delta_{c0}^{(i)})}{\sqrt{1-\cos^2 \delta_c^i}} \frac{\partial \cos(\pi - \delta_c^i)}{\partial \Delta \varphi_i}, \end{cases}$$

with

$$\begin{cases} \frac{\partial \cos(\pi - \delta_b^i)}{\partial \Delta u_i} = \frac{2h_i [\cos(\theta_i + 2C_i \cdot \phi) + 1] r^2 [\cos(\theta_i + C_i \cdot \phi) - \cos(\phi)]^2}{\{h_i^2 + r^2 [\cos(\theta_i + C_i \cdot \phi) - \cos(\phi)]^2\}^2}, \\ \frac{\partial \cos(\pi - \delta_c^i)}{\partial \Delta u_i} = \frac{2h_i [\cos(\theta_i) + 1] r^2 [\cos(\theta_i + C_i \cdot \phi) - \cos(\phi)]^2}{\{h_i^2 + r^2 [\cos(\theta_i + C_i \cdot \phi) - \cos(\phi)]^2\}^2}, \\ \frac{\partial \tan \delta_a^i}{\partial \Delta \varphi_i} = -\frac{h_i}{4r} \frac{\sin(\theta_i + C_i \cdot \phi)}{\sin^2(\theta_i/2 + C_i \cdot \phi) \sin^2(\theta_i/2)}, \\ \frac{\partial \cos(\pi - \delta_b^i)}{\partial \Delta \varphi_i} = -h_i^2 \frac{\sin(\theta_i + 2C_i \cdot \phi) [h_i^2 + r^2 [\cos(\theta_i + C_i \cdot \phi) - \cos(\phi)]^2] + [\cos(\theta_i + 2C_i \cdot \phi) + 1] \{-2r^2 \sin(\theta_i + C_i \cdot \phi) [\cos(\theta_i + C_i \cdot \phi) - \cos(\phi)]\}}{\{h_i^2 + r^2 [\cos(\theta_i + C_i \cdot \phi) - \cos(\phi)]^2\}^2}, \\ \frac{\partial \cos(\pi - \delta_c^i)}{\partial \Delta \varphi_i} = -h_i^2 \frac{\sin(\theta_i) [h_i^2 + r^2 [\cos(\theta_i + C_i \cdot \phi) - \cos(\phi)]^2] + [\cos(\theta_i) + 1] \{-2r^2 \sin(\theta_i + C_i \cdot \phi) [\cos(\theta_i + C_i \cdot \phi) - \cos(\phi)]\}}{\{h_i^2 + r^2 [\cos(\theta_i + C_i \cdot \phi) - \cos(\phi)]^2\}^2}. \end{cases}$$

At the top unit ($i = n$), the mechanical interaction from the next cell vanishes, i.e., $F_{\text{mech}}^{(n+1)} = T_{\text{mech}}^{(n+1)} = 0$.

The equations of motion are numerically solved using an adaptive Runge–Kutta–Fehlberg (RKF45) time integration scheme. The state vector, including generalized displacements and velocities, is advanced in time with adaptive step size control based on local error estimation. The time step is automatically adjusted to satisfy a prescribed tolerance, ensuring numerical stability and efficiency.

5. Parameter Identification and Calibration

This section describes the identification of all material and inertial parameters used in the dynamic simulations described in Section 4. The parameters are determined through a combination of experimental calibration and analytical estimation. Specifically, the elastic stiffness parameters ($k_s^{(i)}$, $k_r^{(i)}$) are calibrated from quasi-static torsional measurements, while the mass and inertia properties (m_i, J_i) are determined using a measurement-based lumped model. The damping factor ν and the magnetic-field ramp-up time are identified through curve fitting, by matching simulated and experimental transient responses during state transitions.

A. Calibration of Stiffness. We determine the stretching stiffness $k_s^{(i)}$ and rotational stiffness $k_r^{(i)}$ for each cell type ($i \in$ {red, yellow, black, white}) through inverse calibration using experimental torsional loading curves. For a single unit cell undergoing torsional deformation with free axial translation, the principle of minimum potential energy yields

$$T_{\text{mech}} = \frac{\partial U_{\text{e}}(u, \varphi)}{\partial \varphi}, \; F_{\text{mech}} = \frac{\partial U_{\text{e}}(u, \varphi)}{\partial u}. \tag{25}$$

We simulate the torsional response of a deployed unit cell ($h_0 = h_{\text{deploy}}$) under free axial translation by minimizing the elastic energy

$$\min_h \; U_{\text{e}}(u, \varphi) \quad \text{s.t.} \quad 0 < h < 1.5 h_{\text{deploy}}, \tag{26}$$

where $h = h_0 + u$. This minimization enforces axial force equilibrium ($F_{\text{mech}} = \partial U_e / \partial u = 0$). For a series of prescribed twist angles $\varphi \in (0, \theta_{\text{deploy}} - \theta_{\text{fold}})$, the resulting equilibrium configurations yield the torque–twist relation $T_{\text{mech}}(\varphi)$ for given stiffness values k_s and k_r.

From each experimental torsional loading curve, we extract four representative quantities:

- Peak torque T_{p}: Maximum torque during snap-through
- Minimum torque T_{m}: Torque at the second stable state (or at minimum if not reached)
- Critical snap-through twist angle φ_{s}: Angle at which snap-through occurs
- Final folded angle φ_{f}: Angle at the second stable (folded) state

The experimental values for the four cell types are summarized in Table S1. Note that the yellow cell did not reach the second stable state during testing due to its low stiffness; thus, φ_{s} and φ_{f} are taken as the angle at minimum torque. For unit cells with opposite chirality, the experimentally measured torque and twist angle naturally exhibit opposite signs under the same Instron loading protocol. In the stiffness calibration, we remove this chirality- induced sign difference by defining all torques and twist angles with respect to the intrinsic folding direction of each unit cell, such that the reported values represent folding magnitudes independent of handedness.

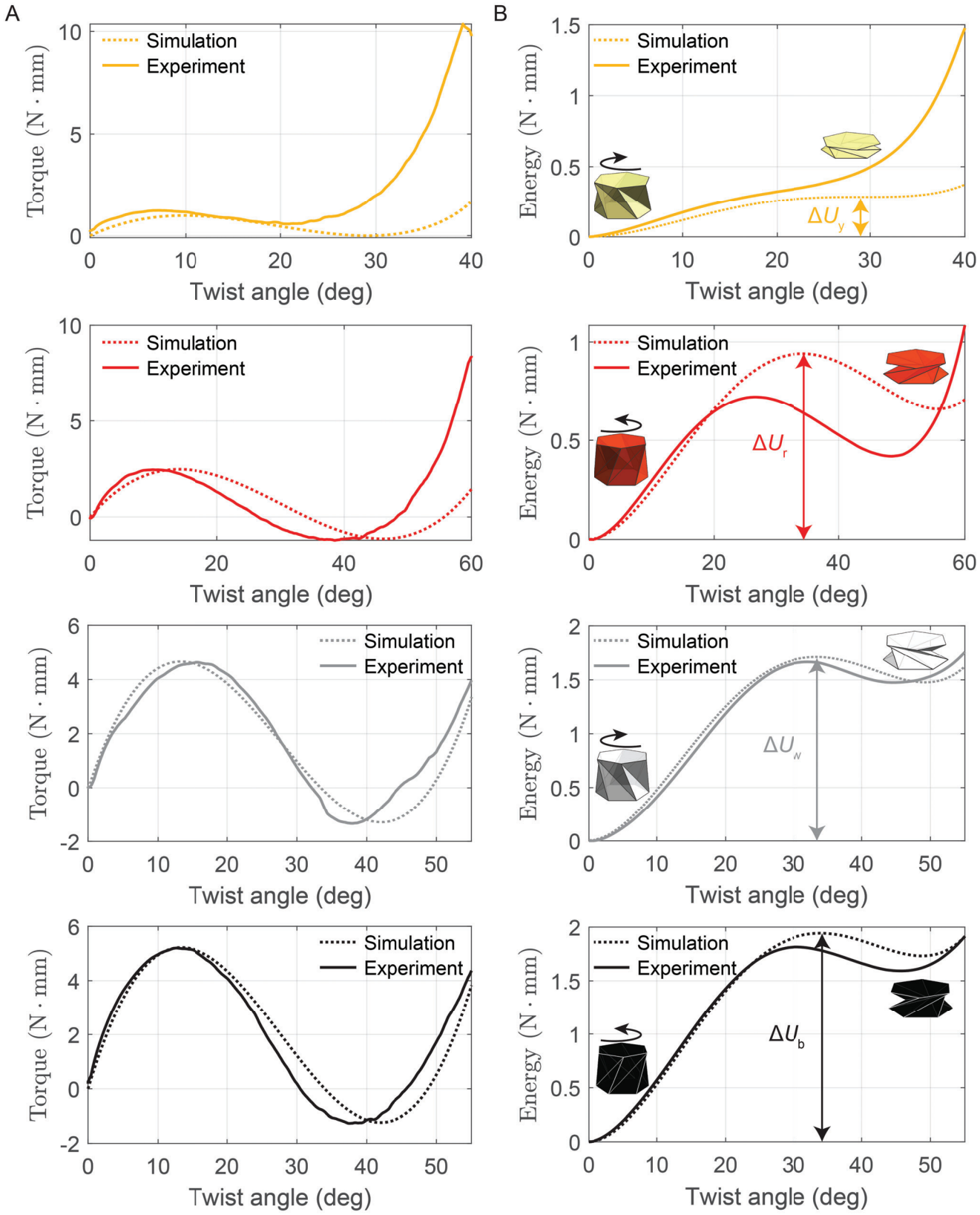


Fig. S7. Comparison of quasi-static torsional experiments and model predictions for four Kresling origami unit cells under free translation. (A) Torque versus twist angle. (B) Elastic potential energy versus twist angle.

We calibrate k_s and k_r by solving the following multiobjective goal attainment problem using MATLAB's `fgoalattain` function

$$\min_{k_s,k_r,\gamma} \ \gamma \quad \text{s.t.} \quad \begin{cases} \mathbf{f}(k_s,k_r) - \mathbf{goal} \le \mathbf{weight}\cdot\gamma, \\ T_{\mathrm{m}}(k_s,k_r) \le 0. \end{cases} \tag{27}$$

where $\mathbf{goal} = [T_{\mathrm{p}}, T_{\mathrm{m}}, \varphi_{\mathrm{s}}, \varphi_{\mathrm{f}}]^T$ contains the experimental target values, and $\mathbf{f}(k_s,k_r) = [T_{\mathrm{p}}^{\mathrm{sim}}, T_{\mathrm{m}}^{\mathrm{sim}}, \varphi_{\mathrm{s}}^{\mathrm{sim}}, \varphi_{\mathrm{f}}^{\mathrm{sim}}]^T$ is obtained by solving Eq. 26 for a range of φ values. For the red, white, and black cells, the weight vector is set as $\mathbf{weight} = [0, 0.001, 1, 1]^T$, which enforces exact matching of the peak torque T_{p} (hard constraint with weight = 0) while preferentially fitting the minimum torque T_{m}. For the yellow cell, snap-through is not resolved in quasi-static measurements due to its low stiffness. The calibration is therefore performed using a reduced objective $\mathbf{f} = [T_{\mathrm{p}}, \varphi_{\mathrm{f}}]^T$, where φ_{f} is obtained from manually folded configurations. The corresponding weight vector is set as $\mathbf{weight} = [1, 0]^T$, enforcing exact matching of φ_{f} while allowing flexibility in fitting T_{p} due to its small magnitude and higher experimental uncertainty.

The calibrated stiffness values for the four cell types are listed in Table S1. Figure S7A shows close agreement between simulated and experimental torque–twist angle curves. The corresponding energy landscapes in Fig. S7B, obtained by integrating the torque–twist angle curves, reveal distinct energy barriers across the four cells ($\Delta U_{\mathrm{y}} < \Delta U_{\mathrm{r}} < \Delta U_{\mathrm{w}} < \Delta U_{\mathrm{b}}$), consistent with their designed stiffness hierarchy (yellow < red < white < black).

B. Calibration of Mass and Moment of Inertia. The inertial parameters of the four-cell origami state machine are determined using a measurement-based lumped model, in which mass is assumed to be concentrated at the polygon plates. The mass of each unit cell type (m_{red}, m_{yellow}, m_{black}, and m_{white}) is measured directly, and each unit cell mass is equally distributed between its top and bottom plates (m_{plate}). The lumped mass associated with an intermediate plate is then taken as the average of the two adjacent unit-cell masses, with the mass of the attached polygon plate included. For the four-cell assembly considered here, the effective mass yields

$$\begin{aligned} m_{\mathrm{red}}^{\mathrm{eff}} &= \frac{m_{\mathrm{red}} + m_{\mathrm{yellow}}}{2} + m_{\mathrm{plate}}, \\ m_{\mathrm{yellow}}^{\mathrm{eff}} &= \frac{m_{\mathrm{yellow}} + m_{\mathrm{black}}}{2} + m_{\mathrm{plate}}, \\ m_{\mathrm{black}}^{\mathrm{eff}} &= \frac{m_{\mathrm{black}} + m_{\mathrm{white}}}{2} + m_{\mathrm{plate}}, \\ m_{\mathrm{white}}^{\mathrm{eff}} &= \frac{m_{\mathrm{white}}}{2} + m_{\mathrm{plate}}. \end{aligned} \tag{28}$$

Under the lumped mass approximation, the mass is represented as a rigid regular hexagon with circumradius r, yielding the effective moment of inertia

$$\begin{aligned} J_{\mathrm{red}}^{\mathrm{eff}} &= m_{\mathrm{red}}^{\mathrm{eff}} \frac{r^2}{6}\left(\sin^2\frac{\pi}{6} + 3\cos^2\frac{\pi}{6}\right), \\ J_{\mathrm{yellow}}^{\mathrm{eff}} &= m_{\mathrm{yellow}}^{\mathrm{eff}} \frac{r^2}{6}\left(\sin^2\frac{\pi}{6} + 3\cos^2\frac{\pi}{6}\right), \\ J_{\mathrm{black}}^{\mathrm{eff}} &= m_{\mathrm{black}}^{\mathrm{eff}} \frac{r^2}{6}\left(\sin^2\frac{\pi}{6} + 3\cos^2\frac{\pi}{6}\right), \\ J_{\mathrm{white}}^{\mathrm{eff}} &= m_{\mathrm{white}}^{\mathrm{eff}} \frac{r^2}{6}\left(\sin^2\frac{\pi}{6} + 3\cos^2\frac{\pi}{6}\right) + m_{\mathrm{magnet}}\frac{1}{2}\left(\frac{d_{\mathrm{magnet}}}{2}\right)^2. \end{aligned} \tag{29}$$

The resulting effective mass and moment of inertia are reported in Table S1.

C. Damping and Actuation Parameters Identification. For the pulsed magnetic actuation, the damping factor ν and the magnetic-field ramp-up time $t_{\mathrm{ramp-up}}$ are identified using the experimentally measured evolution of the normalized total height $h_{\mathrm{tot}}(t)/h_{\mathrm{tot}}(0)$ for transition T1 (Fig. S8). These parameters are then fixed and used to predict the dynamics of all other transitions (T2–T48) without further tuning. We first calibrate the magnetic-field ramp-up time under pulsed magnetic actuation based on experimentally measured current profiles (Fig. S5A), which indicate that the linear ramping stage occurs over a time window of approximately 250–350 ms. Guided by this range, we perform simulations using ramp-up durations of 250 ms, 300 ms, and 350 ms and compare the resulting trajectories with the experimental response (Fig. S8A). As the ramp-up time increases, the simulated trajectories shift progressively along the time axis, reflecting the delayed onset of actuation. Among these cases, the 300 ms ramp-up time yields the best agreement with the experimental trajectory, accurately capturing both the transition timing and overall evolution. Next, the damping factor ν is identified by fitting the post-transition oscillatory dynamics of T1 (Fig. S8B). Simulations are performed with $\nu = 25\,\mathrm{s}^{-1}$, $50\,\mathrm{s}^{-1}$, and $75\,\mathrm{s}^{-1}$, and compared with the experimental trajectory. As ν increases, the rate of energy dissipation increases, leading to progressively faster decay of oscillations and reduced amplitude. The case with $\nu = 50\,\mathrm{s}^{-1}$ provides the best agreement with the experimental response, accurately capturing both the oscillation amplitude and decay rate, whereas $\nu = 25\,\mathrm{s}^{-1}$ underestimates damping (exhibiting overly persistent oscillations) and $\nu = 75\,\mathrm{s}^{-1}$ overestimates damping (leading to overly rapid relaxation).

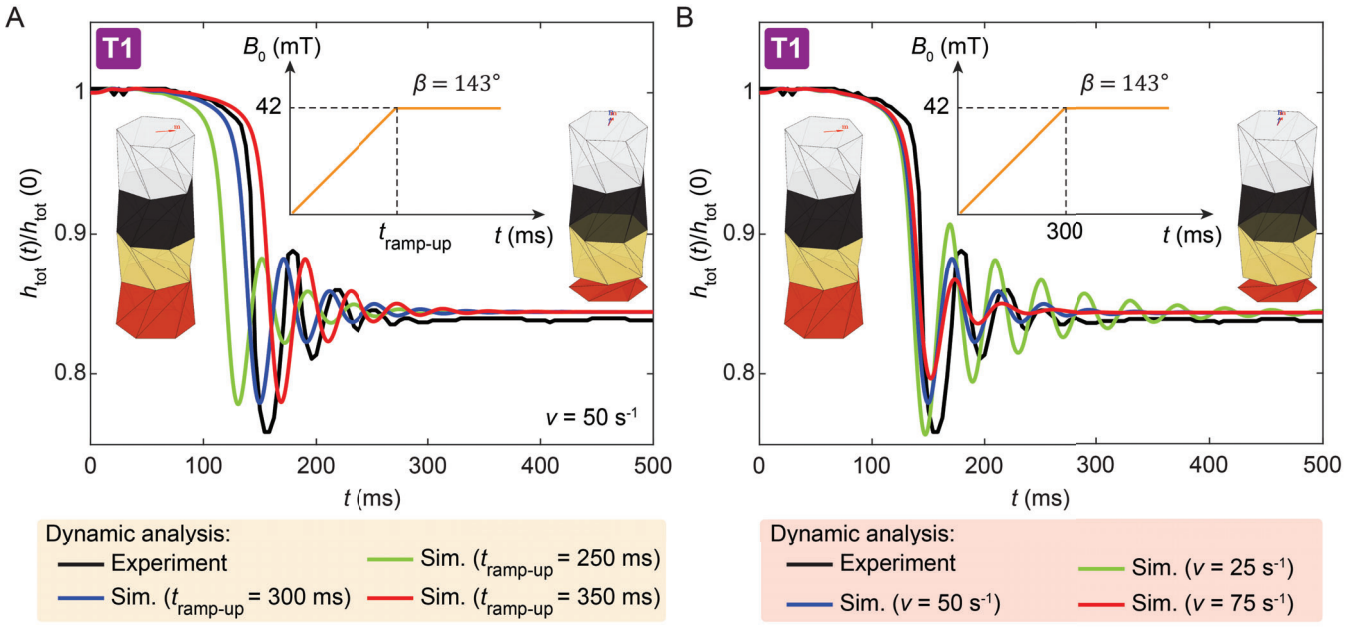


Fig. S8. Identification and sensitivity analysis of actuation and damping parameters under pulsed magnetic actuation T1. (A) Ramp-up time calibration. Simulated trajectories with ramp-up durations of 250 ms (green), 300 ms (blue), and 350 ms (red) are compared with experiment (black). Increasing ramp-up time shifts the response along the time axis, reflecting delayed actuation onset; 300 ms provides the best agreement. (B) Damping factor identification. Simulated trajectories with $\nu = 25\,\mathrm{s}^{-1}$ (green), $50\,\mathrm{s}^{-1}$ (blue), and $75\,\mathrm{s}^{-1}$ (red) are compared with experiment (black). Increasing ν accelerates the decay of oscillations; $\nu = 50\,\mathrm{s}^{-1}$ best captures both oscillation amplitude and decay rate.

The calibrated damping factor is subsequently held fixed for all remaining simulations. Without further parameter adjustment, the model accurately predicts both the pulsed magnetic field-induced dynamics of transition T2 and the rotating-field-induced reset dynamics, accurately capturing the temporal evolution of the normalized total height (Fig. 4C, E of the Main Text) and the top-plate twist angle (Fig. S9). Movie S5 further provides side-by-side experiment–simulation comparisons for representative transitions (T1, T2, the rotating-field reset, and a shortcut transition), demonstrating close agreement in the evolution of individual-cell states. Using the same calibrated parameters, the model also successfully reproduces the experimentally observed state-transition behavior for all remaining pulsed magnetic field-induced transitions (T3–T48) shown in Fig. 2 of the Main Text. The consistent agreement across different actuation protocols, measured trajectories, and individual-cell state evolutions suggests that the phenomenological linear damping formulation (Eq. 21) provides a reasonable approximation of energy dissipation within the operating regime considered in this work.

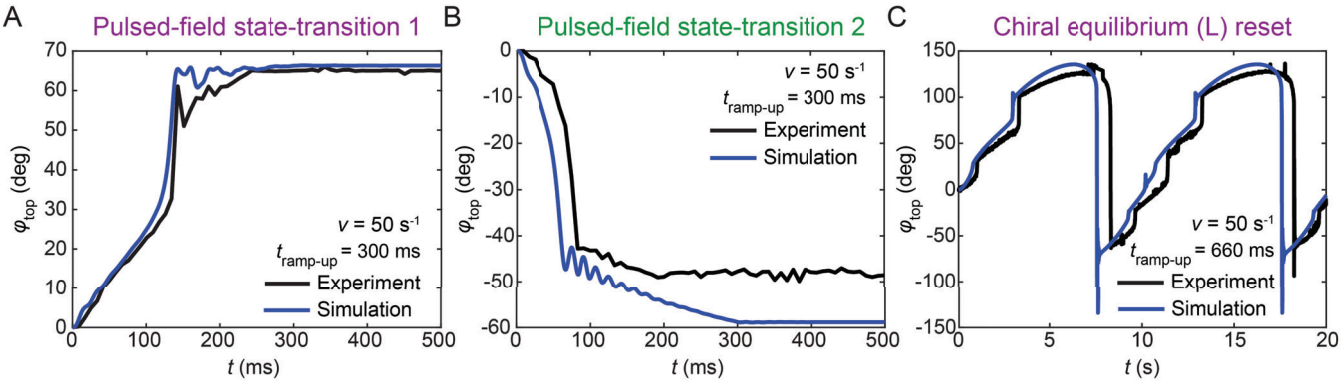


Fig. S9. Comparison of experimentally measured and simulated top-plate twist angles for the pulsed magnetic field-induced transitions T1 (Fig. 4B of the Main Text) and T2 (Fig. 4C of the Main Text), and the rotating-field-induced reset dynamics (Fig. 4E of the Main Text).

To further validate the actuation parameters under rotating magnetic fields, we examine the influence of ramp-up time and actuation frequency on the transient response (Fig. S10). Based on the experimentally measured current profile (Fig. S5B), the ramp-up duration for rotating actuation is approximately 660 ms. This timescale is significantly shorter than the rotation period at $f = 0.1$ Hz ($t = 10$ s), indicating a clear separation of timescales. Consistent with this observation, simulations with ramp-up times of 0 and 660 ms produce nearly identical trajectories (Fig. S10A), demonstrating that the finite ramp-up process has negligible influence on the system dynamics under slow rotating fields. Therefore, the ramp-up time can be effectively approximated as instantaneous in the rotating case.

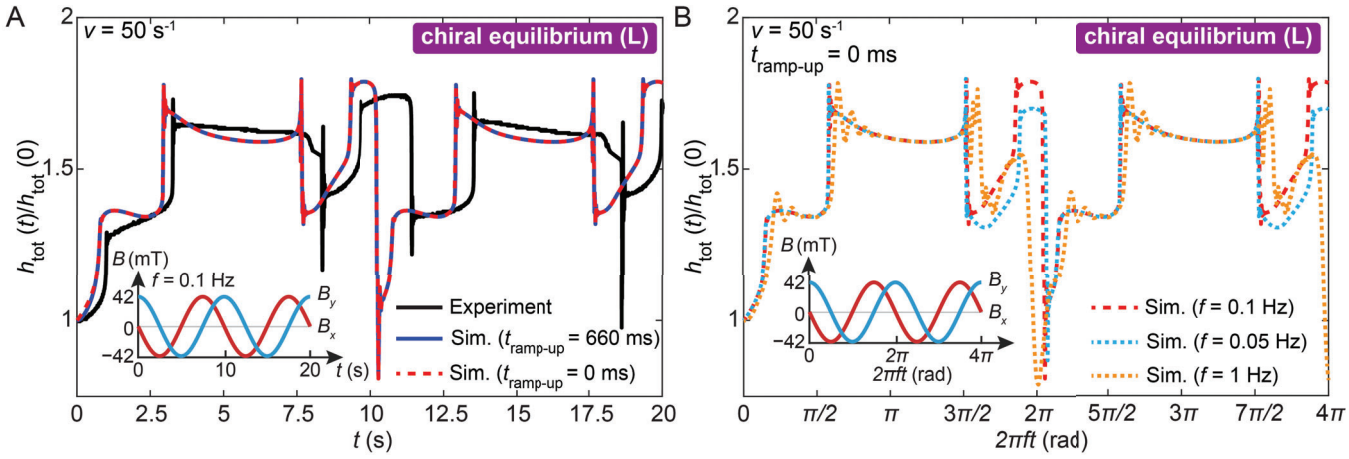


Fig. S10. Identification of actuation parameters under rotating magnetic fields. The normalized height $h_{\mathrm{tot}}(t)/h_{\mathrm{tot}}(0)$ is shown as a function of time (t) or magnetic field angle ($2\pi ft$). (A) Influence of ramp-up time. Simulations with ramp-up times of 0 (red dashed) and 660 ms (blue solid) yield nearly identical trajectories at $f = 0.1$ Hz, indicating that the ramp-up duration is negligible compared to the rotation period (10 s). (B) Influence of rotation frequency. Simulations at $f = 0.05$ (blue dotted), 0.1 (red dashed), and 1 Hz (orange dotted) are compared. At 0.05 and 0.1 Hz, trajectories collapse when plotted against the normalized magnetic field angle. At higher frequency (1 Hz), a delay along the time axis emerges due to finite system response time. A finite and ovelapped equilibrium window is observed across all cases.

We further examine the effect of rotation frequency by comparing simulations at $f = 0.05$, 0.1, and 1 Hz (Fig. S10B). For low frequencies (0.05 and 0.1 Hz), the system exhibits nearly identical behavior when plotted against the normalized time scale defined by the magnetic field angle. At higher frequency (1 Hz), the trajectory exhibits a slight delay along the time axis, reflecting the finite response time of the system. Despite these differences, a finite and overlapped equilibrium window is

consistently observed across all frequencies, demonstrating the robustness of the reset mechanism.

6. Model-Guided Actuation Design of a Five-Cell Origami State Machine

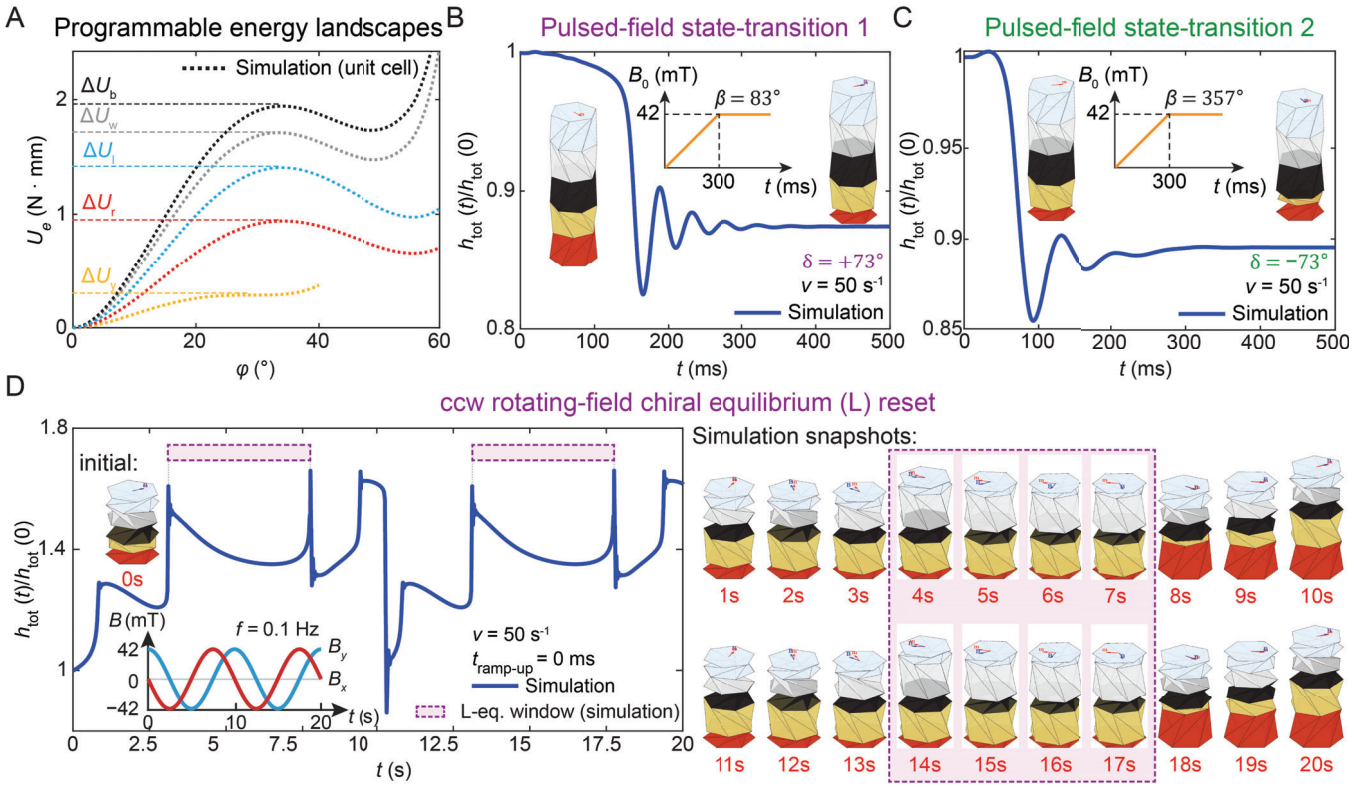


Fig. S11. Model-guided predictive design and control of a five-cell origami state machine. (A) Elastic energy landscapes U_e for the five unit cells used in the simulations. (B,C) Model-guided design of pulsed magnetic actuation for targeted state transitions. Simulated normalized height trajectories $h_{\mathrm{tot}}(t)/h_{\mathrm{tot}}(0)$ are shown for transitions (`11111` $\rightarrow$ `01111`) and (`01111` $\rightarrow$ `00111`). In (B), a L (ccw) torque selectively activates chirality-compatible cells, leading to snap-through of the red cell first; the model identifies a pulsed magnetic field ($B_0 = 42$ mT, $\beta = 83°$) that realizes this transition. In (C), a R (cw) torque drives the yellow cell first, consistent with the designed energy hierarchy and chirality-compatibility; the corresponding actuation field is predicted as ($B_0 = 42$ mT, $\beta = 357°$). (D) Model-predicted behavior under rotating magnetic actuation. The system converges to a L chiral equilibrium state (`01010`) within a finite angular window of the applied field and sequentially traverses distinct intermediate states during continuous rotation, demonstrating programmable state evolution and stability under dynamic driving.

To demonstrate the predictive capability of the model, we apply it to a five-cell origami assembly constructed by extending the four-cell system with an additional (light blue) unit at the top (Fig. S11). The mechanical parameters assigned to this added cell are listed in Table S1. Figure S11A shows the simulated elastic energy landscapes U_e for the five unit cells, highlighting the variation in energy barriers that govern their sequential snap-through behavior (yellow < red < light blue < white < black). These energy profiles with chirality patterning (LH–RH–LH–RH–LH) define the accessible state space and transition pathways of the coupled system.

Figures S11B and C demonstrate model-guided design of actuation protocols for targeted state transitions. Simulated normalized height trajectories are shown for representative pulsed magnetic field-induced transitions (`11111` $\rightarrow$ `01111`) and (`01111` $\rightarrow$ `00111`). In Fig. S11B, a left-handed (L, counterclockwise) torque is applied starting from the fully deployed configuration (`11111`). Based on chirality compatibility, the red, black, and light-blue cells can be activated. Among them, the red cell, designed with the lowest energy barrier, undergoes snap-through first, initiating the transition sequence. Using the predictive model, we identify a pulsed magnetic field ($B_0 = 42$ mT, $\beta = 83°$) that realizes this transition, with the magnetization orientation referenced to 90° at the 00000 state. In Fig. S11C, a right-handed (R, clockwise) torque is applied from configuration (`01111`). Based on chirality compatibility, the yellow, red, and white cells can be activated. Among them, the yellow cell, designed with the lowest energy barrier, undergoes snap-through first, initiating the transition sequence. Using the predictive model, we identify a pulsed magnetic field ($B_0 = 42$ mT, $\beta = 357°$) that realizes this transition under the same magnetization reference. Importantly, deterministic programming of the five-cell assembly is achieved using the same magnetic-field actuation parameters ($B_0 = 42$ mT, $\delta = \pm 73°$) as those used for the four-cell assembly presented in the Main Text (see Fig. 4B, C), demonstrating the robustness of the actuation protocol in larger assemblies with well-separated neighboring energy barriers.

Figure S11D further demonstrates model-guided prediction of system behavior under rotating magnetic actuation. The model predicts both the angular range of the magnetic field over which a stable chiral equilibrium (L-eq.) emerges, and the sequence of intermediate states traversed during continuous rotation. Specifically, the system converges to the chiral equilibrium configuration (`01010`) within a finite equilibrium window in field angle, and sequentially transitions through distinct states as

the field rotates. These results demonstrate that the reduced-order model not only predicts snap-through behavior, but also enables model-guided design of magnetic actuation for deterministic programming in origami assemblies.

Movie S1. Full-state navigation using pulsed magnetic fields.

Movie S2. Cyclic state transitions under rotating magnetic fields.

Movie S3. Universal reset to chiral equilibria with rotating magnetic fields.

Movie S4. Dynamics-enabled shortcuts & stepwise programming.

Movie S5. Snap-through dynamics: experiment & simulation.

Movie S6. *StateMorph*: origami state machine-enabled robot with adaptive locomotion.

References

1. S Zang, D Misseroni, T Zhao, GH Paulino, Kresling origami mechanics explained: Experiments and theory. *J. Mech. Phys. Solids* **188**, 105630 (2024).
2. K Manos, et al., Wireless actuation of magnetic robots with a modular 60 mt 3-d helmholtz coil system in *2025 IEEE Applied Power Electronics Conference and Exposition (APEC)*. (IEEE), pp. 1274–1278 (2025).
3. JJ Abbott, E Diller, AJ Petruska, Magnetic methods in robotics. *Annu. Rev. Control. Robotics, Auton. Syst.* **3**, 57–90 (2020).
4. K Liu, GH Paulino, Nonlinear mechanics of non-rigid origami: an efficient computational approach. *Proc. Royal Soc. A: Math. Phys. Eng. Sci.* **473** (2017).
5. D Yan, BF Aymon, PM Reis, A reduced-order, rotation-based model for thin hard-magnetic plates. *J. Mech. Phys. Solids* **170**, 105095 (2023).
6. J Safko, H Goldstein, C Poole, Classical mechanics (2002).
7. H Yasuda, et al., Origami-based impact mitigation via rarefaction solitary wave creation. *Sci. Adv.* **5**, eaau2835 (2019).